

Physical processes in laser ablation into liquid and laser shock wave pinning

V A Khokhlov¹, N A Inogamov^{1,2}, V V Zhakhovsky^{2,1}, Yu VPetrov^{1,3}
and S I Anisimov¹

¹ Landau Institute for Theoretical Physics of the Russian Academy of Sciences, Akademika
Semenova 1a, Chernogolovka, Moscow Region 142432, Russia

² Dukhov Research Institute of Automatics (VNIIA), Sushchevskaya 22, Moscow 127055,
Russia

³ Moscow Institute of Physics and Technology, Institutskiy Pereulok 9, Dolgoprudny, Moscow
Region 141701, Russia

E-mail: v_a_kh@mail.ru

Abstract. The most important modern laser technologies include (1) the generation of colloid nanoparticles (NPs), laser ablation into a liquid (LAL—laser ablation in liquid) and (2) surface hardening of products by laser pinning (LSP—laser shock peening). Significantly, with laser pinning, the surface to be treated is washed with water. Therefore, the physics of processes during ablation into a liquid and during pinning is common. True, the accents are different. If the ablation in the liquid actually forget about the shock wave (SW) generated by the impact, and leaving the thickness of the target, in the problem with pinning, on the contrary, the main question is about the impact. In addition, the role of water in (1) and (2) is different. In (1) fluid contributes to the formation of NPs and adopts NPs, gently slowing them. Whereas in (2) water is needed to enhance the recoil and increase the amplitude of the hydrocarbon in the product. The complete picture, developed in the work, of course, should include both edges: and the formation of ejection into the liquid as a result of ablation—i.e. (1), observation of the SW wave from the nucleation stage to its attenuation in the product volume, i.e. (2).

1. Introduction.

Laser action has long been used to generate shock waves in condensed matter. The traditional branch of these applications is to clarify the equations of state (EOS) at high energy densities that are unattainable with chemical explosives [1]. The other branch is connected with the modern technology of laser pinning. With the help of pinning significantly (tens, hundreds of percent [2]) increase resistance to wear (fatigue failure) and resistance to corrosion. For example, strengthen the details of aircraft engines [3, 4].

In this paper, we want to draw attention to significant common phenomena for such different technologies as laser pinning and ablation in liquid. At the same time, the relevant scientific communities are largely disconnected. Similar experiences are interpreted differently. In pinning experiments, crater formation is associated with residual plastic deformations (ablation is neglected), see, for example, [5]. Whereas in experiments with ablation, it is believed that a crater is formed due to the entrainment of a substance into a liquid [6], i.e. the mechanics of the deformation of a solid below the surface of the crater are neglected. Meanwhile the pulse duration of the nanosecond, and the intensity comparable 1–10 GW/cm² in both technologies;

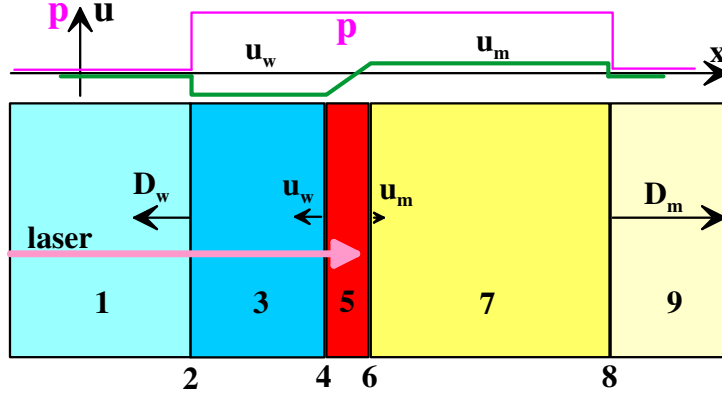


Figure 1. Heating metal through water—arrow “laser”. The model [12] is presented. The laser passes through unperturbed water 1, crosses the shock wave front 2, passes through the shock-compressed water 3 and is absorbed in the hot layer 5. The pulse is long in time (“subsonic” heating) in the sense that the sound scale L/c_s is much shorter than the pulse duration τ_L , here L is the width of the layer 5. Therefore, the boundaries 4 and 6 of layer 5 act as two subsonic pistons pushing waves 2 and 8. Waves 2 and 8 propagate much faster than the expansion rate of layer 5. Therefore, layer 5 is thin compared with layers 3 and 7.

to enhance the effect usually work in the area of the optical breakdown of the liquid. The aluminum target was used in [5], while [6] considered a corundum target; the deformation of brittle materials, which include corundum, is difficult [7].

Of course, understanding the physics of the phenomena taking place is important for successful work. In many ways, this understanding is based on analytical solutions that are complemented by numerical calculations. In the introductory part of this paper, we turn our attention to analytics related to the ablation into water and pinning problems. These analytical solutions describe the expansion into vacuum and condensed matter, long and short pulses. Below is a short list of solutions. In the 70-90s of the XX-th century, a detailed analytical theory of the plasma laser corona was developed in the approximation of a stationary flow and a fixed degree of ionization [8,9]. This solution considers the expansion of the substance in the corona into a vacuum; the energy absorbed in the region of critical density is transmitted by the electronic thermal conductivity to the ablation front, which moves along a relatively cold dense substance.

In the case of ultrashort laser pulses (USLP, there is no transition to a stationary flow) and/or during the expansion into a condensed (not vacuum and not gas) environment, the analyst, of course, changes qualitatively (compared to the plasma corona). A simple thermo-acoustic solutions to help the understanding and implementation of the first estimates, for the case of the impact of USLP on thin films is given in [10]; thin film is considered, the laser warm-up time of which $t_T \sim d_f^2/4\chi$ throughout the thickness is less than the time $t_s = d_f/c_s$, for which the sound runs through the thickness; duration of τ_L of the pulse is small $\tau_L < t_T$; here and below d_f is the film thickness, χ is the thermal diffusivity of the film, c_s is the speed of sound.

The analytical approach in the case of USLP and ablation into the liquid [11] is based on the classical solution of the decay of the gas-dynamic gap: at $t < 0$ we have two half-spaces in contact with each other, at $t = 0$ the separating wall is removed. Substances in half-spaces have different pressure values and at $t < 0$ they rest. In the case of long pulses $\tau_L \gg d_T/c_s$, the analyst of heating of an absorbing target through a transparent dielectric is completely different [12], here d_T is the thickness of the heating layer. Figure 1 presents the corresponding scheme. Below we describe this scheme in detail and compare it with the results of our numerical calculations.

2. On the heating layer supporting nonlinear acoustic waves.

Figure 1, taken from [12], shows a wide area of acoustic perturbation from x_2 to x_8 . It is created by a long-lasting laser pulse. The width of $x_8 - x_2$ is approximately $(c_w + c_m)(t - t_{\text{ini}})$. The time t will be counted from the maximum of the laser pulse with a Gaussian profile $I = I_0 \exp(-t^2/\tau_L^2)$. The moment of the pulse in numerical calculation denote t_{ini} ; we have $t_{\text{ini}} = -3\tau_L$.

Sound velocities in water and metal are c_w and c_m . For absorbable intensities $I_{\text{abs}} \sim 1 \text{ GW/cm}^2$ and durations $\tau_L \sim 1 \text{ ns}$ the pressure to the end of the pulse of the order of 1 GPa. These pressures are small compared to the bulk metal module $B_m \sim 10^2 \text{ GPa}$ and of the order of the water module $B_w = 1.5 \text{ GPa}$. Therefore, the acoustic perturbation running through the water in figure 1, is moderately nonlinear and weakly nonlinear in metal.

The pistons 4 and 6 create a simple Riemann waves, respectively, in water and metal. Focusing of characteristics and wave breaking of the Riemann is happening in the water early due to the high nonlinearity of the waves in the water. In the linear acoustic approximation, the pressure and velocity are connected via the acoustic impedance $p = zu$. In the model [12], the pressure is uniform over the interval from x_2 to x_8 , see the graph in the upper part of figure 1. Then the water velocities u_w and metal u_m are homogeneous, each in its own domain, i.e. in 3 and 7. The expansion rate of the hot layer is $\dot{L} = (1/z_w + 1/z_m)p$. In the numerical calculations below, we consider a pair of gold and water. Acoustic impedance of water is small: $z_w l_m$. So $\dot{L} \approx p/z_w$.

The above relation $\dot{L} = p/z_w$ follows from the acoustic approximation. A difficult place is to establish a balance of energy. Energy supply to the hot layer 5 (arrow ‘‘laser’’ in figure 1), firstly, heats the substance of the layer and, secondly, transfers energy to acoustic waves in water and metal. In [12] this balance is written as:

$$I - p\dot{L} = (d/dt)(E_{\text{int}}L). \quad (1)$$

That is, the intensity absorbed in the layer minus the mechanical work of the pistons is spent on increasing the internal energy E_{int} of layer 5. In this case, it is assumed that new portions of the substance do not enter layer 5; i.e., layer 5 is created at an early stage, and then its mass does not change. It is necessary to link the energy E_{int} and the pressure p , generated by heating in layer 5. Then the equation (1) will allow us to express the pressure p through the intensity I .

In the model [12], the following assumptions are made. The internal energy of E_{int} is divided into two terms: $E_{\text{int}} = E_T + E_{\text{ion}}$, where $E_T = \alpha E_{\text{int}}$ is the thermal energy that determines the pressure of p , and $E_{\text{ion}} = (1 - \alpha)E_{\text{int}}$ is the energy that is spent on the ionization of the substance in layer 5 and is not involved in the pressure increase p . Thus, the effective increase of heat capacity during ionization is taken into account. It is assumed that the coefficient α is constant. In addition, it is assumed that $p = (2/3)E_T$, as in the case of a monatomic ideal gas. Under these assumptions, for a constant laser pulse we obtain:

$$p = \sqrt{\frac{2\alpha}{2\alpha + 3}} z_w I = 5.5 \sqrt{\frac{\alpha}{2\alpha + 3}} \sqrt{\frac{I}{1 \text{ GW/cm}^2}} \text{ GPa}, \quad (2)$$

$$u_w = p/z_w = 3.7 \sqrt{\frac{\alpha}{2\alpha + 3}} \sqrt{\frac{I}{1 \text{ GW/cm}^2}} \text{ km/s}. \quad (3)$$

Here z_w is the water impedance; in numerical estimates (2, 3) the value $z_w = 1 \text{ km/s} = 1 \mu\text{m/ns}$ is substituted, so during the time of the order of $\tau_L \sim 1 \text{ ns}$ the hot layer will expand to the thickness $L \sim 1 \mu\text{m}$. According to [12], the coefficient α is small (~ 0.1), and therefore significant.

3. Heating, expansion and acoustic radiation: the role of melting.

We present the results of numerical simulation of the problem described by the approximate analytical model in the section above. Consider a gold-water pair. Laser radiation passes through water and is absorbed in gold. The corresponding code was described in [10, 11], see

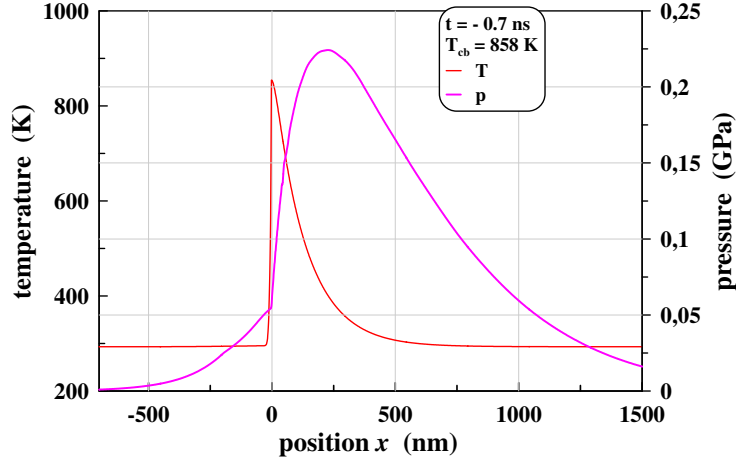


Figure 2. The situation at stage I, i.e. before melting, is shown. The calculation is started at $t_{\text{ini}} = -1.5$ ns. At this point, gold is to the right of the plane $x = 0$, and water is to the left. The initial temperature of water and gold $T_{\text{rt}} = 300$ K. The heat spreads to gold at a depth of $d_T = 0.1 \mu\text{m}$. In the plane at a depth of d_T the temperature is $(T_{\text{max}} - T_{\text{rt}})/2 + T_{\text{rt}} = (T_{\text{max}} + T_{\text{rt}})/2$, i.e. $d_T = 0.1 \mu\text{m}$ is the full width at half-height by temperature increase. The pressure profile has smooth acoustic wings on the left and right.

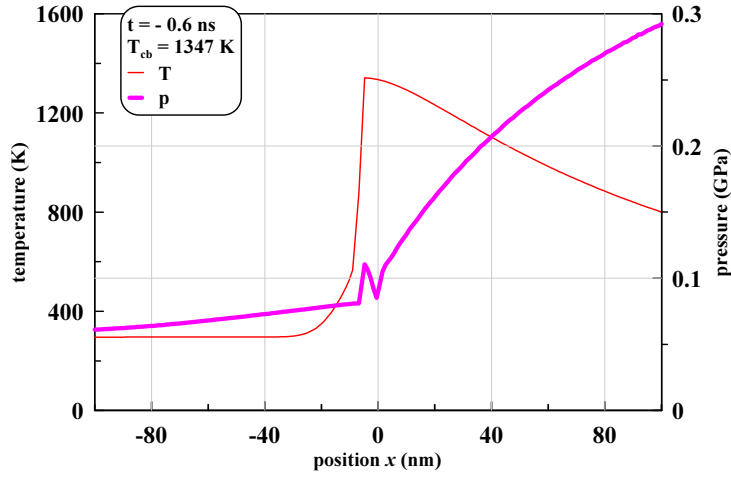


Figure 3. Beginning of stage II with a layer of melt. The contact temperature $T_{\text{cb}} = 1347$ K by 5 degrees surpassed the melting point $T_{\text{m}}(p)$ of gold under a pressure of 943 bar in the region of the contact boundary (cb). The dependence of $T_{\text{m}}(p)$ is shown in the following two figures. At the moment of formation of the liquid phase, a tooth is formed on the pressure profile p in the contact area. At stage I, the p profile is smooth everywhere—there are no teeth anywhere.

also [13–17]. The pulse shape has the form $I = I_0 \exp(-t^2/\tau_L^2)$, $\tau_L = 0.5$ ns, the absorbed energy is 0.9 J/cm^2 .

The flow in its development goes through a number of stages. The first is stage I, where the solid metal is heated. This stage ends when the melting of the metal begins. This is followed by stage II, in which the melt layer expands, and its temperature on contact with water increases. At the end of stage II, the temperature of the metal on the contact reaches a critical temperature of gold. In stage III, a gaseous layer of metal is formed near the contact. Stage IV refers to the end of the heating pulse. At this stage, a deep dip in the pressure profile begins to form. This

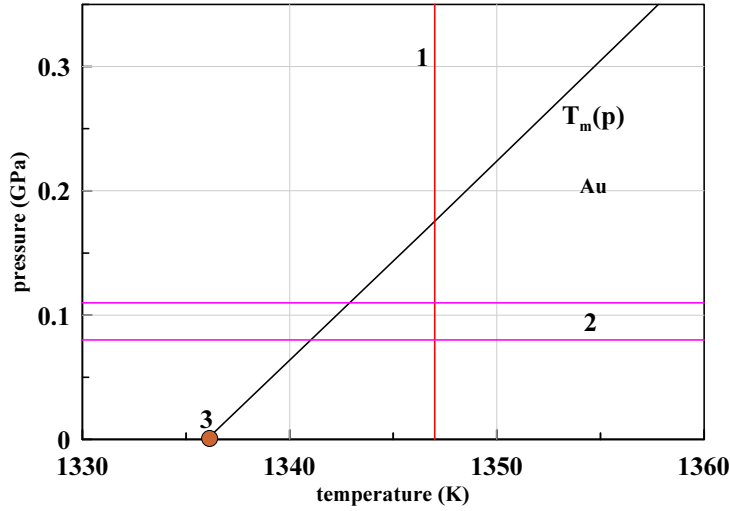


Figure 4. A small segment of the melting curve on the plane T, p is presented. This is the segment near the triple point marked with marker 3. A more complete phase diagram in the pressure range of interest is shown in the following figure 5. At the triple point, the melting point of gold (Au) is 1337 K. The amplitude of the tooth pressure, taken from figure 3, shown by lines 2. Contact temperature $T_{cb} = 1347$ K in figure 3 marked vertical line 1. This temperature corresponds to the time $t = -0.6$ ns. As you can see, the temperature $T_{cb} = 1347$ K is 5 degrees higher than the melting point $T_m(p = 943 \text{ bar}) = 1342$ K. The pressure of 943 bar corresponds to the average pressure between horizontal lines 2.

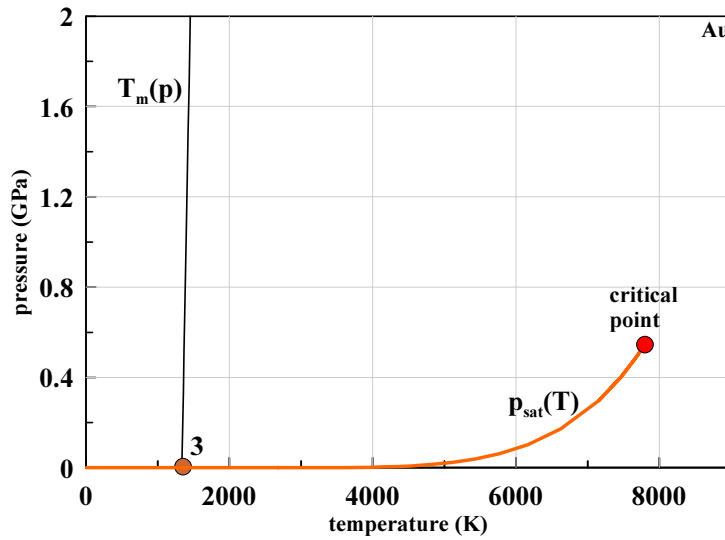


Figure 5. The figure shows the melting curve $T_m(p)$ or $p_m(T)$ and the dependence of the saturated vapor pressure on the temperature $p_{sat}(T)$. The data are taken according to the equation of state developed in the [18–23]. Marker 3 marked a triple point. The dependence $p_{sat}(T)$ ends at the critical point with the parameters 7800 K, 5300 bar and 5.3 g/cm^3 [18–23]. The vapor pressure at the triple point is negligible $p_{sat}(T = 1337 \text{ K}) = 4.3 \times 10^{-8} \text{ bar}$; the concentration of gold atoms in a vapor is $2.3 \times 10^{11} \text{ cm}^{-3}$. The boiling point is $p_{sat}(T = 3243 \text{ K}) = 1 \text{ bar}$.

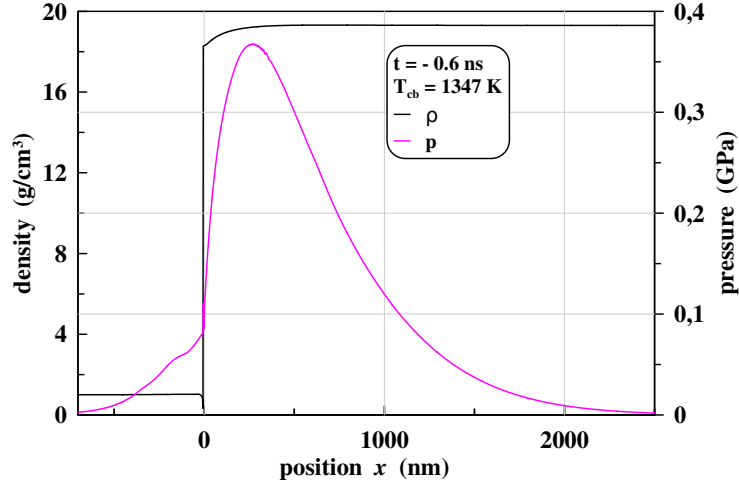


Figure 6. The density and pressure profiles at the same time point as shown in figure 3. Acoustic perturbations (simple Riemann waves running into the water and into gold) outside the wave of pressure are smooth functions of the coordinate. Tooth in figure 3 on the scale of x , adopted in this figure, is a very narrow splash at $x \approx 0$.

dip is in the contact area. The appearance of the dip is due to the termination of heating of the contact area and the divergence in the direction of the acoustic perturbation formed during the action of the laser pulse.

Let us illustrate the above with respect to the stages of the process. Let's start with stage I and its transition to stage II. The figure 2 shows the instantaneous temperature and pressure profiles shortly before the end of the stage I—the laser heats the metal, but the metal temperature remains below the melting temperature, for gold $T_m = 1337$ K. The thickness of the heated layer of metal $d_T = 0.1 \mu\text{m}$. If we estimate this thickness by the formula $2\sqrt{\chi(t_{\text{obs}} - t_{\text{ini}})}$, we get about $0.7 \mu\text{m}$; here $\chi \approx 1.2 \text{ cm}^2/\text{s}$ is the temperature conductivity of solid gold, $t_{\text{obs}} = -0.7$ is the time point at which the graphs in figure 2, $t_{\text{ini}} = -1.5$ ns—the time when the code starts to work. It is clear that the estimate of $2\sqrt{\chi\Delta T}$ does not work, because the wing of the time intensity distribution $I \propto \exp(-t^2/\tau_L^2)$ is very weak in the time interval near the moment of the beginning of the calculation t_{ini} . Indeed, if t_{ini} is carried away to minus infinity, then this estimate will give an infinite thickness of the heated region, whereas the profiles in figure 2 practically will not change.

Pressure profile in figure 2 has smooth spatial wings on the left in water and on the right in gold. These are acoustic perturbations associated with the time-axis left wing of the time profile of the laser pulse $I \propto \exp(-t^2/\tau_L^2)$, on which the intensity increases with time. Perturbations propagate along the characteristics with speed of sound in water and the gold of layer heating. The laser energy is absorbed in the skin layer of the metal near the gold-water contact boundary. Acoustic disturbances are created due to temperature growth and thermal expansion of the substance in the heated layer with the current thickness of the order of d_T .

The contact boundary reaches the melting temperature T_m at the time moment $t \approx -0.6$ ns, see figure 3 and pictures 4, 5; to better understand the melting, the phase diagram of gold is shown in the figures 4, 5. Formation of a tooth on a pressure profile in figure 3 associated with the appearance of the liquid phase and with the difference scheme used. Outside the tooth, the pressure profile remains smooth, see figure 6. A similar detail with profile strengthening due to the beginning of melting was observed earlier in the works [24] (see figure 6 and 7 in this article), [25] (see figure 2 and 3 in this article; melting imprint in the profile of a simple Riemann

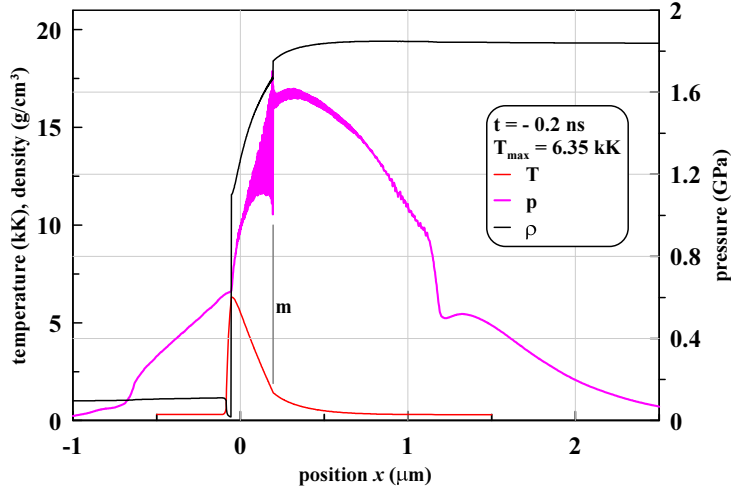


Figure 7. The middle of stage II (melting stage). The melting front is marked by the vertical m. The strong heating of gold with a laser continues, the contact temperature is 6.35 kK, the melt thickness is a quarter of a micron. Because of the heating, the pressure increases with time and the pressure profile looks like a mound with a maximum slightly to the right of the heating layer, cf. from figure 1. Two step sections with high pressure gradients are clearly visible on the pressure profile. They are at $x = -0.6 \mu\text{m}$ and $x = 1.2 \mu\text{m}$. Behind these areas, the p profile smoothly falls outward from the contact. The outer portions are acoustic waves emitted from the heating layer in stage I (i.e. before melting). Tilting of simple Riemann waves on steep sections due to the focusing characteristics leads to the nucleation of shock waves on these sections. Focusing is due to non-linear effects in simple waves. Rollover occurs later in time with respect to the moment of time $t = -0.2 \text{ ns}$, shown in this figure.

wave profile), [26]. All these articles are devoted to ultrashort laser pulses when heating occurs isochorically. Then the melting section between solidus and liquidus is imprinted in the profiles of temperature and pressure. Then this spot begins to travel according to acoustic characteristics.

The work [27] also observed the strengthening of the Riemann simple wave profile, which (strengthening) is emitted from the melting front when the melting zone is switched from supersonic to subsonic propagation. If the works [24–26] are based on the hydrodynamic code, then [27] is used molecular dynamics (MD). In MD, melting proceeds as in nature. Ie MD automatically takes into account the possible real effects of the melting nonequilibrium; in hydrodynamic modeling there is no disequilibrium, an equilibrium equation of state is used. In the MD pressure profiles, the melting site is smoothed, but remains noticeable. And if in [24–26] the plastic equation of state of matter in the solid phase is used (there are no elastic shock waves) [18–23], then MD [27–35] clearly shows the elastic-plastic transition; a detailed experimental and theoretical studies of elastic–plastic transition in ultrashort loading were carried out in the works of Ashitkov, Kanel, Agranat, etc. [36–38], see also [39,40]. It turns out [27], that there is a superposition of two effects (A) of the ablation imprint of melting on the characteristics and (B) of the formation of an elastic shock wave. The strengthening of the acoustic profile section by melting accelerates the formation of an elastic shock wave—the simple Riemann wave is tilted earlier because of the presence of a steeper section.

Figure 7 shows the density, temperature, and pressure profiles at time $t = -0.2 \text{ ns}$. At this point, the gold absorbed 29% of the laser pulse energy, i.e. 29% of 0.9 J/cm^2 . The thickness of the gold melt layer in figure 7 is $0.25 \mu\text{m}$. At stage II, shown in figure 7, the laser continues actively heat gold in the heating layer d_T . This heating increases and raises the pressure in the

layer d_T . Therefore, the pressure profile has the form of a bump with a maximum slightly to the right of the heating layer d_T . On the right and left acoustic wings a trace from the beginning of melting is clearly visible. The specified trace (or imprint), as discussed above for ultrashort pulses, has the form of a section with a steeper pressure stroke.

Oscillations running to the right and to the left of the melting front are associated with the error of the difference scheme. Oscillations propagate along the characteristics. The calculation uses a one-dimensional hydrodynamic code with division into steps (cells) at the Lagrangian coordinate x^0 , see [10, 11, 13–17]. The partition pitch (the length of the Lagrangian cell) is Δx^0 uniform over the integration interval. In the described calculation, $\Delta x^0 = 1$ nm is assumed. The time step is 10 fs. The velocity of the melting front on matter is $u_m = 400$ m/s in the considered time interval. This means that the melting front one step (one cell) along the Lagrangian grid passes over a time interval $\Delta t_m = \Delta x^0 / u_m = 2.5$ ps. At this moment, the state of matter in the cell Δx^0 changes abruptly from the state of the solid phase to the state of the liquid phase.

One more time. Consider a cell that is adjacent to the melting front but not yet melted. It remains in a solid state 250 steps in time. And then literally in one step in time passes into the liquid phase. This transition creates an oscillation due to the density difference in the solid and liquid phases; as the cell expands, passing into the liquid. Further, this oscillation is carried by the characteristics departing from the melting front to the right and to the left. The spatial length of the oscillation is $\Delta t_m c_s \approx 5$ nm at the speed of sound in gold at a melting temperature of about 2 km/s.

We note that in the case of a relatively long (subsonic) laser pulse considered here with $\tau_L = 0.5$ ns, the melting front is just the front. Its thickness is equal to the width of a single Lagrangian cell Δx^0 . If we reduce the pitch Δx^0 , then the oscillation length will be proportionally reduced; of course, the step can be greatly reduced so that the melting front is blurred into a transition zone with varying phase composition. The sharpness of the transition between the phases means that the melting process is described quite well in the approximation of the Stefan problem. In this sense, the subsonic laser pulse is qualitatively different from the “supersonic” pulse. The latter corresponds to the ultrashort pulse. The impulse becomes supersonic when $\tau_L < d_T / c_s$. In the opposite case, the pulse was named above slow or subsonic. In the supersonic case, there is a transition zone of sufficiently Lagrangian cells of mixed composition, in which the solid and liquid phases coexist [24–26]; therefore, in the case of ultrashort exposure, there are no such pronounced oscillations as in figure 7. The composition gradually changes from pure solid to pure liquid at the edges of the transition zone.

The presence of oscillations is associated with the difference character of approximation. As one moves away from the melting front, the oscillation amplitude decreases. The first oscillation, which was formed at the time of the beginning of melting (shown in the figures 3, 4 and 6), remains pronounced at subsequent points in time, see, for example, fig 7. In figure 7 step sections on the pressure profile correspond to this oscillation. There are two such sites. At the moment of $t = -0.2$ ps, one of them is in water at $x \approx -0.6$ μm , while the second is in gold at $x \approx 1.2$ μm , see figure 7. The speed of sound in gold is greater, so the area in gold is located farther from the contact. The subsequent several oscillations, which were emitted by the melting front after the first, have already attenuated substantially. Their amplitude is small compared with recently emitted oscillations.

Due to the expansion of the metal during melting, a velocity jump occurs at the melting front. The amplitude of the jump is approximately $\Delta u_m \approx 20$ m/s. With the acceleration of the substance at the intersection of the melting front, the existence of a small pressure jump at the front is connected. Speed and pressure jumps are shown in figure 8. The pressure jump amplitude is $\Delta p_m \approx 0.18$ GPa. The velocity of the melting front relative to the substance is about $u_m \approx 400$ m/s. At the melting front, conservation laws are fulfilled. The Rayleigh line $\Delta p_m = j \Delta u_m$ follows from the conservation of mass and momentum; here $j = \rho u$, u is the

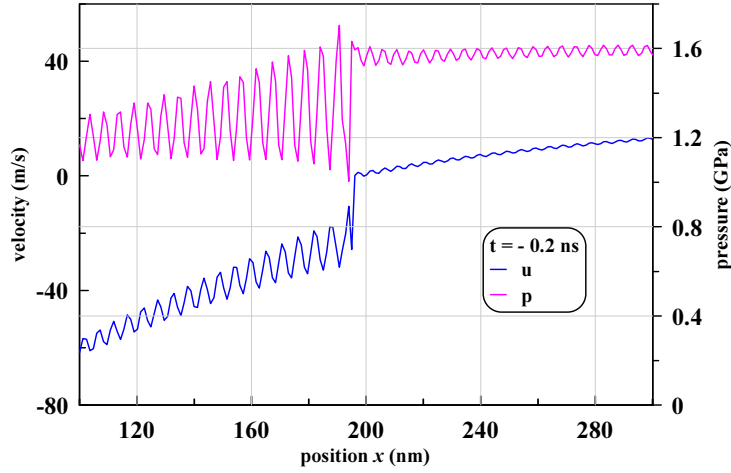


Figure 8. The jump associated with the melting front separates the liquid phase on the left and the solid phase on the right. The relation between the jump amplitudes and the direct Rayleigh is discussed in the text. The movement of the melting front is subsonic, the Mach number is about 0.17.

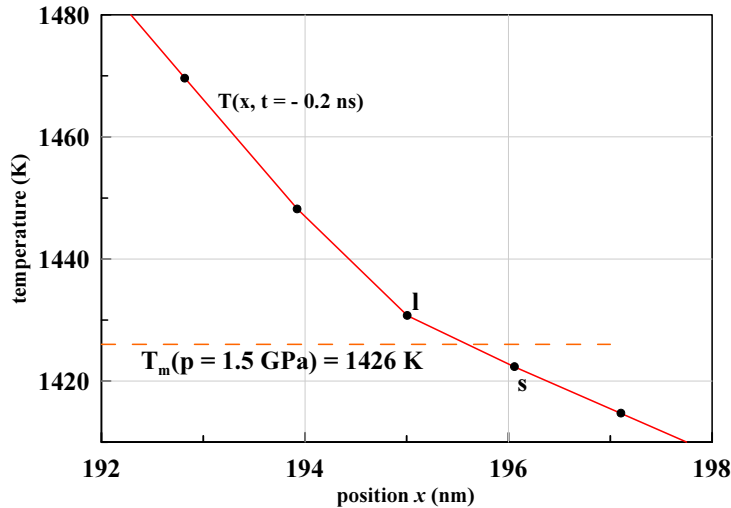


Figure 9. Temperature distribution over Lagrangian nodes/cells near the melting front at time-0.2 ns. Explanations regarding the jerks of state from solid to liquid and relative to the temperature gradient are given in the text. The state changes when the node s (solid phase) reaches a melting point of 1426 K. This is the melting point at a pressure of 1.5 GPa in the vicinity of the melting front, see figure 8.

velocity of matter relative to the front, i.e. u_m . The values of Δp_m , Δu_m and u_m from our calculation satisfy the relation that is the direct Rayleigh.

Figure 9 shows the portion of the temperature profile near the melting front. On the profile, points mark the division points into Lagrangian cells. Direct 1426 K gives the melting point according to the melting curve $T_m(p)$. This curve is shown in the figures 4 and 5. The melting point of 1426 K is reached at a pressure of 1.5 GPa. The pressure value of 1.5 GPa in the region of the melting front at the time $t = -0.2$ ns is taken from figure 8.

The temperature difference between points s (solid phase) and l (liquid phase) in figure 9

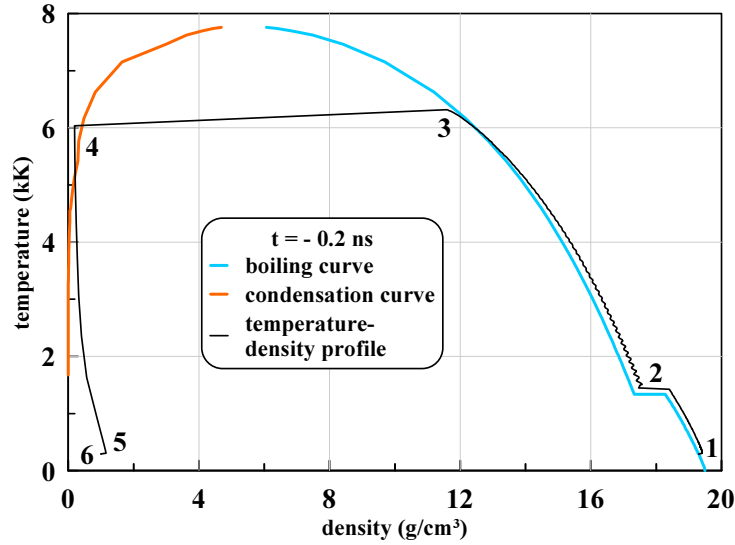


Figure 10. The state of matter in the phase diagram at time point of -0.2 ns. Together with the phase equilibrium curves, the density and temperature profiles are constructed in parametric form: $\rho(x, t = -0.2 \text{ ns}), T(x, t = -0.2 \text{ ns})$. The parameter that runs through the profile is the coordinate x . Points 1-6 refer to: 1—undisturbed gold deep in the target, 2—melting front repeating the density jump at the triple point (figure 7–9), 3—maximum temperature on contact with water (figure 7), 3–4—density jump from gold to water (figure 7), 4—hot water adjacent to the contact, 4–5 temperature profile in water, 6—water far from the contact. Of course, the states of water are irrelevant to the gold condensation curve. Under the influence of the pulse, the temperature of gold rises. Therefore, point 3 rises higher and higher along the boiling curve. However, there is no gold evaporation, since the pressure is higher than the saturated vapor pressure, see figure 5. Evaporation will start when point 3 reaches the critical point. This issue is devoted to the next section of work.

is equal to 8 K. The temperature in the Lagrangian cell s grows at a rate of 0.03 K in one integration step over time. Over the order of 100 time steps, the temperature in the Lagrangian cell s will exceed the melting point of 1426 K. At the same time, the cell will change its status—it will turn from solid to liquid (melt). The formation of the next oscillation is due to such melting jerks.

The temperature gradient is higher in the liquid phase, see figure 7 and 9. Two factors determine this effect. First, melting occurs at this stage. I. e., new and new portions of solid gold are melted. In order to cover the costs associated with the latent melting heat Q , it is necessary that the heat flux q_l to the front exceed the heat flux q_s from the front: $q_l - q_s = Q\rho_s u_m$, where Q —the heat of fusion per unit mass. Secondly, the coefficient of thermal conductivity is about 2–2.5 times lower in the liquid phase; the thermal conductivity model used in the calculation takes into account the change in thermal conductivity during melting. Therefore, even at $Q = 0$, the temperature gradient will be higher in the liquid.

In the case of long pulses, the resulting pressure is small (compared with the bulk modulus of the metal). Therefore, the substance is located along the boiling curve in accordance with the temperature distribution in gold, see figure 10; the boiling curve is called the right branch of the binodal (phase coexistence curve). I. e., the extension of matter is mostly due to the heat. The available pressure has little effect on the density (in the sense of deviation from the boiling curve). In figure 11 the hydrodynamic profile is compared with the boundaries of the phase transitions of the first kind on the plane ρ, p . We see that on shown in figure 11 the moment of

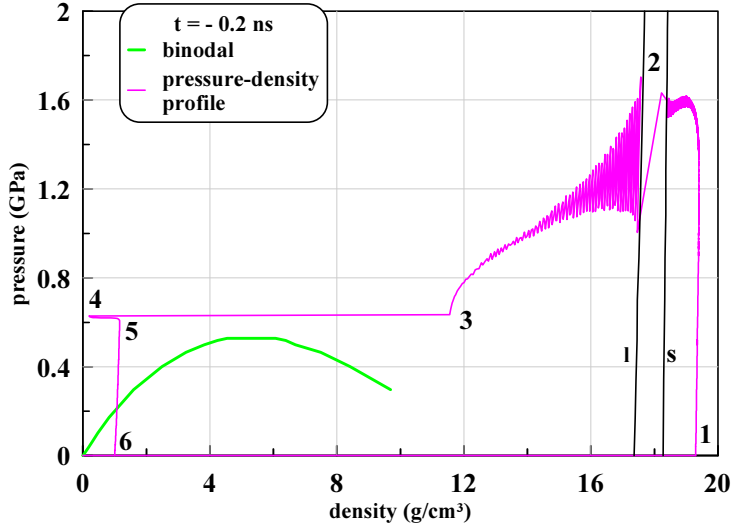


Figure 11. Here, the hydrodynamic profile is built together with the phase equilibrium curves on the ρ, p plane. The numbers 1–6 indicate the same states as in the previous figure 10. We see that the pressure at the hottest point of gold is still above the critical pressure of gold. The hottest is point 3. It is on contact with water. The letters s (solidus) and l (liquidus) indicate melting curves bordering the corridor of the existence of a mixture of solid and liquid phases. The intersection of this corridor with the instantaneous profile of the density and pressure distributions corresponds to segment 2 in figure 10. The pressure at the intersection of the melting front abruptly decreases, cf. with pictures 7 and 8

time all gold (points 1–2–3) is still located to the right of the critical density of gold 5.3 g/cm^3 . Additional heating is needed to exceed the critical temperature (see figure 10) and lower the density below the critical value (see figure 11).

4. The excess of the critical temperature of gold, the appearance of a contact layer of gaseous gold.

Over time, the temperature of the metal near the contact rises under the action of the laser. As mentioned above, the flow in its development goes through several stages: stage I ends with the start of melting; stage II is completed with the achievement of the critical temperature of the metal. At stage III, three layers are adjacent to the metal contact with water. With the transition from stage II to stage III begins the formation of a layer of gold in the gaseous state. So at stage III, a layer of gaseous gold is located near the contact, then a layer of melt follows, and then there is a solid phase.

Figures 12–15 show the situation at time $t = 0$. Stage III begins: the contact temperature exceeds the critical temperature $T_{\text{cr}} = 7.8 \text{ kK}$, and the density falls below the critical value $\rho_{\text{cr}} = 5.3 \text{ g/cm}^3$. But the pressure is about 4 times the critical value of $p_{\text{cr}} = 0.53 \text{ GPa}$. As is known, the density range $\rho < \rho_{\text{cr}}$ is related to the gas phase. At a density of $\rho > \rho_{\text{cr}}$, the substance is assumed to be in the liquid phase. Of course, above the critical point such a division is conditional. A substance at $\rho \sim \rho_{\text{cr}}$ is called a fluid or nonideal gas. We are talking about the gaseous state, not the gas state, in the case of nonideal gas. Although in the case shown in figure 12–15, the gold pressure in the gas layer between the boundaries 2 and 3 in figure 13 is close to the pressure given by the formula for the ideal gas $p = nk_B T$ for the density and temperature in this layer. Note that according to used in the calculation of the equation of state of gold [18–23], compressibility factor of $p/(nk_B T)$ is equal to 0.3 at the critical point.

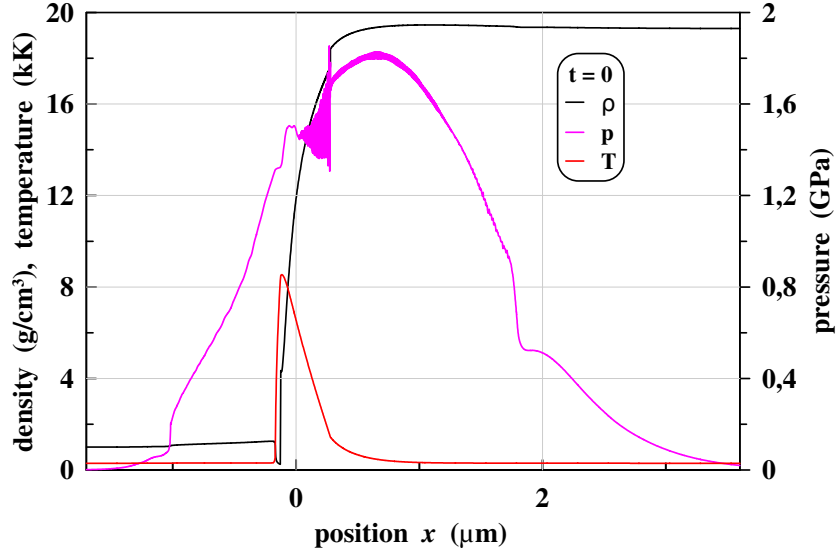


Figure 12. Profiles of density, temperature and pressure at time $t = 0$. The pressure profile contains information about changes in the intensity of the laser pulse over time. The moment $t = 0$ is close to the moments of overturning of simple waves in water and gold: the steep sections on the pressure profile are close to the vertical segments at the points of inflection. By the time $t = 0$, gold absorbed half the energy $F_{\text{abs}}/2$ of the incident pulse $I(t) = I_0 \exp(-t^2/\tau_L^2)$. In the calculation described in this paper, we have: $\tau_L = 0.5$ ns, $F_{\text{abs}} = 900$ J/cm². At $t > 0$, the intensity of $I(t)$ decreases as compared with the maximum value of I_0 .

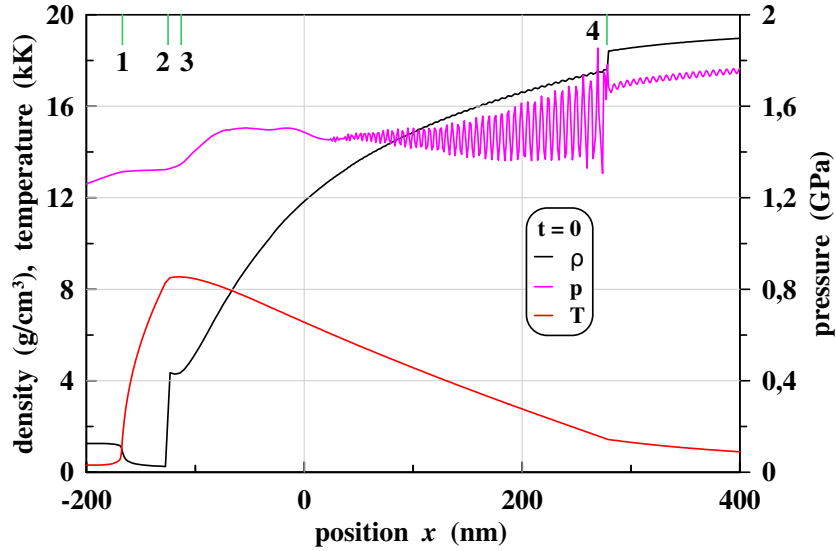


Figure 13. The structure of the contact zone at $t = 0$ is shown. Strips 1, 2, 3 and 4 mark the boundaries of the layers. To the left of 1 is cold dense water, the thermal conductivity of water is calculated from the data taken from the literature. Between the boundaries 1 and 2 there is a layer of hot partially dissociated water, 2—gold—water contact. The equation of state of water is taken from [41]. Layer 2–3 is gaseous gold. Layer 3–4 occupies the liquid phase, 4—the melting front, it moves relative to the substance to the right. To the right of 4 is the solid phase.

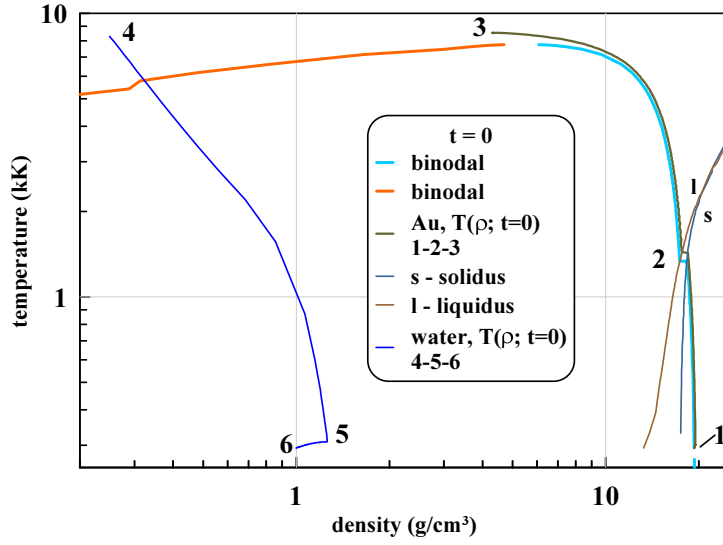


Figure 14. Temperature profile $T(\rho; t = 0)$ on the phase plane ρ, T . The gradual heating by the laser leads to the fact that the temperature on the profile $T(\rho; t = 0)$ rises above the critical value $T_{cr} = 7.8$ kK. The single (for water and Au) profile $T(\rho; t = 0)$ is divided into two 1–2–3 (Au) and 4–5–6 (water) pieces. A density jump of 3–4 refers to the contact boundary, cf. from figure 10, where a single profile is shown. Au and water densities at the contact are 4.35 and 0.25 g/cm³. Curves s (solidus) and l (liquidus) are continued through the triple point to the metastable area [18–23]. Point 1 corresponds to gold at a great distance from the contact, where the temperature is equal to room emperature 300 K.

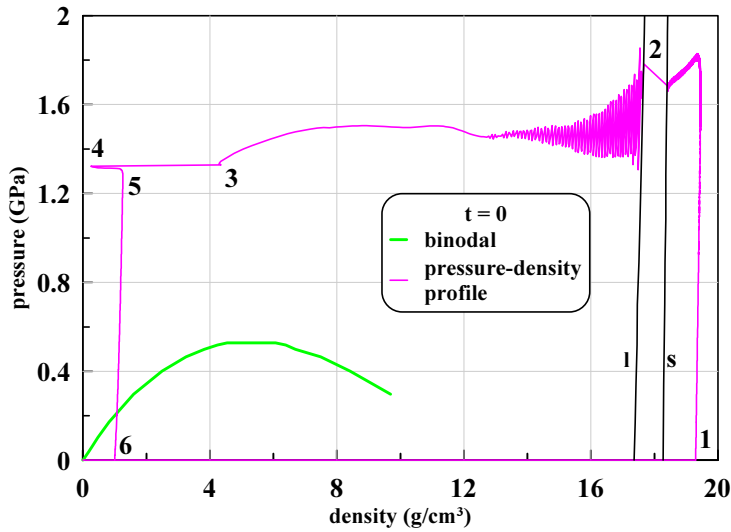


Figure 15. Pressure profile $p(\rho; t = 0)$ on the phase plane ρ, p . For the time elapsed from the previous time point $t = -0.2$ ns, see figure 11, the pressure has increased significantly. The maximum pressure is in the solid phase behind the melting front. The meaning of numbers 1–6 is the same as in figures 10, 11 and 14. Note that the 1–2–3 profile, which was just above the boiling curve in figure 14 and 10, here it is far removed from the boiling curve. This is due to the low compressibility of the condensed phase.

By the time point $t = 0$ gold absorbed half the energy F_{abs} of the pulse. From the figures 12–15 it follows that the gas layer of gold 2–3 (see figure 13) is formed at the moment $t \approx 0$. The coincidence with the maximum of the pulse $\tau_L = 0.5$ ns, $F_{\text{abs}} = 900$ J/cm² occasional. Indeed, if the energy of F_{abs} were greater, then the achievement of the gas state would occur before the maximum pulse $I \propto \exp(-t^2/\tau_L^2)$.

In figure 14 layers are shown: 1–2 hot water, coordinates $x = -167$ and -125 nm, thickness 42 nm; a layer of gas gold 2–3 with coordinates -125 and -113 nm, thickness 12 nm and a layer of melt almost 400 nm thick. The melting front coordinate at time $t = 0$ is 278 nm. The coordinates of x are measured from the initial position of the contact boundary.

We emphasize that in the gas state layer 2–3 in figure 13 falls around the critical point from above. That is, the layer 2–3 is not formed as a result of evaporation of the heated condensed matter. Pressure in the region 1–2–3 in figure 13 above the saturated vapor pressure $p_{\text{sat}}(T)$. This pressure is above the maximum value that the function $p_{\text{sat}}(T)$ can have, i.e. above the critical pressure p_{cr} , see figures 5 and 15. Layer 2–3 in figure 13 is formed as a result of continuous temperature growth on the temperature profile $T(x, t)$ of gold over time t during the action of the laser pulse: $T(x^0, t_2) > T(x^0, t_1)$, if $t_2 > t_1$, here x^0 —Lagrangian coordinate. On the phase plane ρ, T this profile is located along the melting curve, see figures 10 and 14. To the instantaneous profile $T(x, t), \rho(x, t)$ there correspond points: 1 (state far in volume)—2 (melting front)—3 (contact) in the figures 10 and 14.

Due to the increase in temperature at the contact, the top point 3 of the profile $T(x, t), \rho(x, t)$ moves up along the melting curve, cf. figures 14 and 10. Point 3 in the figures 14 and 10 reaches the critical value $T_{\text{cr}} = 7.8$ kK and then (with continued heating) it begins to exceed this value if the energy input F_{abs} is large enough. The temperature profile $T(\rho; t)$ in figure 14 goes slightly above the boiling curve, because the pressure is higher than $p_{\text{sat}}(T)$.

Let the saturated vapor above the liquid phase form as a result of the evaporation of this liquid. Then there are two states on the phase plane ρ, T : one on the boiling curve and the other on the condensation curve. The pressure in the vapor–liquid system is equal to the saturated vapor pressure $p_{\text{sat}}(T)$, see figure 5. In our situation, as it is said, evaporative formation of a layer of pure gold vapor (without water) is impossible until the condition $p > p_{\text{sat}}(T)$ is satisfied.

Compare the number of gold atoms that have passed the gas–vapor phase by evaporation (path B) and by heating above the critical temperature point $T_{\text{cr}} = 7.8$ kK by ΔT of the order of one or several thousand degrees (path A). The evaporation of gold atoms into water takes place even in the profile situation shown in figure 10. The corresponding number of evaporated atoms N_B is small compared to the number of atoms N_A in interlayer 2–3 in figure 13. In our code with the Lagrangian coordinate x^0 there are no mixed cells in which both gold atoms and water molecules would be present. Therefore, the processes of evaporation into water and mutual diffusion are not taken into account. A molecular dynamics approach [15] is required to analyze these processes.

As mentioned, the figures 12–15 show the situation at the time $t = 0$ of the laser pulse maximum. Then the intensity absorbed in the metal begins to decrease with time. However, the growth of the temperature and pressure maxima $T_{\text{max}}(t), p_{\text{max}}(t)$ continues for some time, that is, these maxima are shifted in time relative to the intensity maximum $I(t)$. Stage IV starts when the formation of a dip in the pressure profile begins. The following section is devoted to this topic.

5. Emission of acoustic disturbances from the heating layer.

Acoustic disturbance tracing the history of heating $I(t) : I(t) \rightarrow T(x \sim 0, t) \rightarrow p(x \sim 0, t) \rightarrow p(x \pm ct)$, where $x \sim 0$ is the area of heating, the letter c with the plus sign is the wave going into the water. At the same time, C is the speed of sound in water. Similarly, c minus refers to the wave propagating in gold. Fig 16 shows the development of the acoustic field at the final

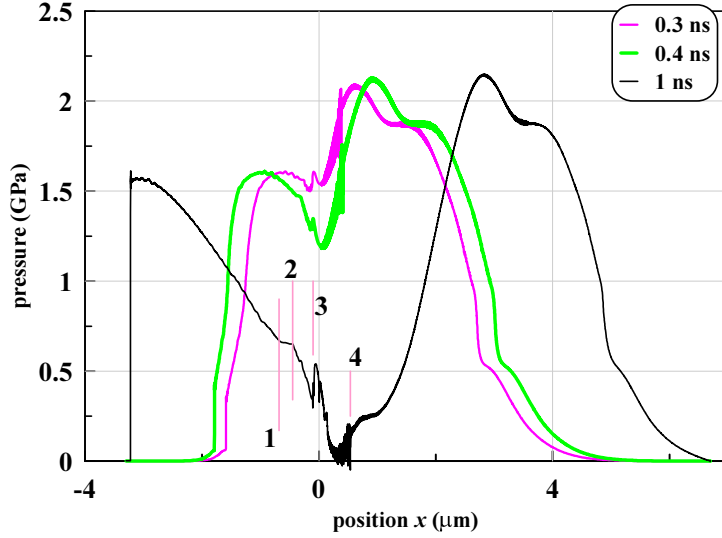


Figure 16. Evolution of the pressure field after the start of a decrease of the absorbed laser pulse intensity $I(t) \propto \exp(-t^2/\tau_L^2)$, $t > 0$. Recall that $\tau_L = 0.5$ ns. At times about $t \approx 0.3$ ns, the formation of a dip in the pressure profile begins due to a decrease in the rate of heating of the substance. At $t \approx 1$ ns there is a complete separation of waves running to the left (into the water) and to the right (into gold). Points 1, 2, 3 and 4 mark the boundaries of the layers. As in figure 13, these are the boundaries of the hot water layer 1–2, the gaseous gold layer 2–3 and the melt layer 3–4 at the time $t = 1$ ns.

stages of laser action, when the intensity of $I(t)$ decreases.

The increase in the maximum temperature of $T_{\max}(t)$ (over the instantaneous temperature field) continues at $t > 0$, despite the decrease in the intensity of $I(t)$. Indeed, energy is still being supplied to the system. A slow decrease in the value of $T_{\max}(t)$ begins at $t \approx 0.4$ ns when the thermal conductivity losses begin to exceed the laser heating power. The highest temperature in space and time $T_{\max-x,t}$ is 11.3 kK for the considered laser pulse. Radiation losses $\sigma_{\text{SB}}T^4 \sim 10^9$ W/m² in the considered range of times and temperatures are small in comparison with the electron heat flux in the metal $\kappa dT/dx \sim 10^{12}$ W/m² at $\kappa \sim 100$ W/m/K, $dT \sim 8$ kK, $dx \sim 300$ nm.

At $t \approx 0.3$ ns the formation of a dip on the pressure profile $p(x, t)$ in the area of the heating layer begins. This is shown in figure 16. The temperature rise in the heating region dT/dt first slows down and then stops. Accordingly, the thermal expansion of gold stops. Namely, this expansion is associated with an increase in pressure in the heating region, which is emitted from this area by acoustic characteristics.

The beginning of stage IV is connected with the moment of time $t \approx 0.3$ ns with the formation of a dip in the p profile. Gradually, a single pressure bump breaks up into two different waves extending into gold and water, see figure 16. Herewith the pressure in the contact zone is reduced to a pressure that is determined by heated gold and hot water.

A shock wave is formed from a steep section in the water in figure 16; the existence of two steep sections was discussed in figures 7 and 12; this is the transition from stage I to stage II. The volumetric water module of 2.25 GPa is almost two orders of magnitude lower than the gold module of 180 GPa. Therefore, the tilting of a steep section in water occurs much earlier than in gold. Although the water pressure is slightly lower than gold, see figure 16. In the shock wave, the heating history of $I(t)$ gradually disappears, reflected in the $p(x \pm ct)$ profile of the Riemann simple wave. Gradually, the wave transforms into a triangular shock wave, cf. the

profiles at time points of 0.3 and 0.4 ns with the profile at time of 1 ns in figure 16.

The evolution of the shock wave in the metal is important for laser pinning. For pinning, it is necessary that (i) a shock wave be formed in the metal and (ii) that the amplitude of this wave be above the elastic limit. Then an elastic-plastic wave propagates into the metal. Plastic deformations remaining behind the front of a plastic wave are due to the hardening of the surface layer of the product with respect to fatigue failure and corrosion. The solution of the problem of elastic-plastic wave is beyond the scope of this presentation. The complexity here is in the end-to-end consideration of the elastic-plastic behavior together with the phenomena of phase transitions of the first kind: melting/crystallization and condensation. Previously, this problem was solved for the case of ultrashort pulse: see work with molecular dynamics [27, 29–31], as well as hydrodynamic studies in which multiphase and phase transitions are embedded together with elasto-plasticity [33, 42, 43].

6. Conclusion.

In connection with the applications associated with the formation of colloids of nanoparticles and laser pinning, the earlier stages of the action of a nanosecond pulse on a gold target in water have been poorly studied. Thermophysical processes of formation and emission of simple Riemann waves from the heating region are considered. The history of the contact zone is investigated: gradual heating of gold and water: the formation of a hot water layer and a hot gold layer.

References

- [1] Anisimov S I, Prokhorov A M and Fortov V E 1984 *Phys. Usp.* **27** 181
- [2] Karthik D and Swaroop S *Mater. Manuf. Processes* **32** 1565–72
- [3] wikipedia.org/lsp.technologies URL https://en.wikipedia.org/wiki/LSP_Technologies
- [4] lsp.technologies URL <https://www.lsp.technologies.com/history.php>
- [5] Correa C, Peral D, Porro J A, Díaz M, de Lara L R, García-Beltrán A and Ocaña J L 2015 *Opt. Laser Technol.* **73** 179 – 187
- [6] Lam J, Lombard J, Dujardin C, Ledoux G, Merabia S and Amans D 2016 *Appl. Phys. Lett.* **108** 074104
- [7] Dyachkov S A, Parshikov A N, Egorova M S, Grigoryev S Yu, Zhakhovsky V V and Medin S A 2018 *J. Appl. Phys.* **124** 085902
- [8] Sanz J, Linan A, Rodriguez M and Sanmartin J R 1981 *Phys. Fluids* **24** 2098–106
- [9] Sanz J 1994 *Phys. Rev. Lett.* **73** 2700–3
- [10] Inogamov N A, Zhakhovskii V V and Khokhlov V A 2015 *J. Exp. Theor. Phys.* **120** 15–48
- [11] Inogamov N A, Zhakhovskii V V and Khokhlov V A 2018 *J. Exp. Theor. Phys.* **127** 79–106
- [12] Fabbro R, Fournier J, Ballard P, Devaux D and Virmont J 1990 *J. Appl. Phys.* **68** 775–84
- [13] Khokhlov V A, Inogamov N A, Zhakhovsky V V and Petrov Yu V 2018 Formation of solitary microstructure and ablation into transparent dielectric by a subnanosecond laser pulse arXiv:1811.11990 [cond-mat.mes-hall]
- [14] Petrov Yu V, Khokhlov V A, Zhakhovsky V V and Inogamov N A 2018 Laser-induced ablation of metal in liquid arXiv:1812.09109 [physics.comp-ph]
- [15] Petrov Yu V, Inogamov N A, Zhakhovsky V V and Khokhlov V A 2018 Condensation of laser produced gold plasma during expansion and cooling in water environment arXiv:1812.09929 [physics.comp-ph]
- [16] Khokhlov V A, Petrov Yu V, Inogamov N A, Migdal K P, Winter J, Aichele C, Rapp S and Huber H P 2018 *J. Phys.: Conf. Ser.* **1147** 012066 (arXiv:1811.10312 [cond-mat.mes-hall])
- [17] Inogamov N A, Khokhlov V A and Zhakhovsky V V 2018 *JETP Letters* **108** 439
- [18] Bushman A V, Fortov V E, Kanel G I and Ni A L 1993 *Intense Dynamic Loading of Condensed Matter* (Taylor & Francis Translation, London)
- [19] Khishchenko K V, Tkachenko S I, Levashov P R, Lomonosov I V and Vorob'ev V S 2002 *Intern. J. Thermophys.* **23** 1359–67
- [20] Lomonosov I V 2007 *Laser Part. Beams* **25** 567–84
- [21] rusbank URL <http://teos.ficp.ac.ru/rusbank/>
- [22] rusbank URL <http://www.ihed.ras.ru/rusbank/>
- [23] Povarnitsyn M E, Andreev N E, Apfelbaum E M, Itina T E, Khishchenko K V, Kostenko O F, Levashov P R and Veysman M E 2012 *Appl. Surf. Sci.* **258** 9480 – 3

- [24] Inogamov N A, Zhakhovskii V V, Ashitkov S I, Khokhlov V A, Yu V Petrov, Komarov P S, Agranat M B, Anisimov S I and Nishihara K 2009 *Appl. Surf. Sci.* **255** 9712–6 (arXiv:0812.2965 [physics.optics])
- [25] Inogamov N A, Ashitkov S I, Zhakhovskiy V V, Shepelev V V, Khokhlov V A, Komarov P S, Agranat M B, Anisimov S I and Fortov V E 2010 *Appl. Phys. A* **101** 1–5
- [26] Inogamov N A, Zhakhovskiy V V, Ashitkov S I, Khokhlov V A, Shepelev V V, Komarov P S, Ovchinnikov A V, Sitnikov D S, Petrov Yu V, Agranat M B, Anisimov S I and Fortov V E 2011 *Contrib. Plasma Phys.* **51** 367–74
- [27] Demaske B J, Zhakhovskiy V V, Inogamov N A and Oleynik I I 2013 *Phys. Rev. B* **87** 054109
- [28] Agranat M B, Anisimov S I, Ashitkov S I, Zhakhovskii V V, Inogamov N A, Komarov P S, Ovchinnikov A V, Fortov V E, Khokhlov V A and Shepelev V V 2010 *JETP Lett.* **91** 471–7
- [29] Zhakhovskii V V and Inogamov N A 2010 *JETP Lett.* **92** 521–6
- [30] Inogamov N A, Zhakhovskiy V V, Khokhlov V A and Shepelev V V 2011 *JETP Letters* **93** 226–32
- [31] Zhakhovskiy V V, Budzevich M M, Inogamov N A, Oleynik I I and White C T 2011 *Phys. Rev. Lett.* **107** 135502
- [32] Perriot R, Zhakhovskiy V V, Inogamov N A and Oleynik I I 2014 *J. Phys.: Conf. Ser.* **500** 172008
- [33] Il'nitskiy D K, Khokhlov V A, Inogamov N A, Zhakhovskiy V V, Petrov Yu V, Khishchenko K V, Migdal K P and Anisimov S I 2014 *J. Phys.: Conf. Ser.* **500** 032021
- [34] Ashitkov S I, Zhakhovskiy V V, Inogamov N A, Komarov P S, Agranat M B and Kanel G I 2017 *AIP Conf. Proc.* **1793** 100035
- [35] Zhakhovskiy V V, Migdal K P, Inogamov N A and Anisimov S I 2017 *AIP Conf. Proc.* **1793** 070003
- [36] Ashitkov S I, Agranat M B, Kanel' G I, Komarov P S and Fortov V E 2010 *JETP Lett.* **92** 516–520
- [37] Kanel G I, Zaretsky E B, Razorenov S V, Ashitkov S I and Fortov V E 2017 *Phys. Usp.* **60** 490–508
- [38] Kanel' G I, Garkushin G V, Savinykh A S and Razorenov S V 2018 *J. Exp. Theor. Phys.* **127** 337–341
- [39] Whitley V H, McGrane S D, Eakins D E, Bolme C A, Moore D S and Bingert J F 2011 *J. Appl. Phys.* **109** 013505
- [40] Crowhurst J C, Armstrong M R, Knight K B, Zaug J M and Behymer E M 2011 *Phys. Rev. Lett.* **107** 144302
- [41] Nigmatulin R I and Bolotnova R Kh 2011 *High Temperature* **49** 303–6
- [42] Khokhlov V A, Inogamov N A, Zhakhovskiy V V, Anisimov S I and Petrov Yu V 2014 *Proceedings of the Kabardino-Balkarian State University* **4**(1) 53–59
- [43] Inogamov N A, Zhakhovskiy V V, Khokhlov V A, Demaske B J, Khishchenko K V and Oleynik I I 2014 *J. Phys.: Conf. Ser.* **500** 192023